ACS NANO
www.acsnano.org

ARTICLE

Wafer-Scalable Single-Layer Amorphous Molybdenum Trioxide

Md Hasibul Alam, Sayema Chowdhury, Anupam Roy, Xiaohan Wu, Ruijing Ge, Michael A. Rodder, Jun Chen, Yang Lu, Chen Stern, Lothar Houben, Robert Chrostowski, Scott R. Burlison, Sung Jin Yang, Martha I. Serna, Ananth Dodabalapur, Filippo Mangolini, Doron Naveh, Jack C. Lee, Sanjay K. Banerjee, Jamie H. Warner, and Deji Akinwande*

Cite This: *ACS Nano* 2022, 16, 3756–3767 Read Online

ACCESS | Metrics & More | Article Recommendations | Supporting Information

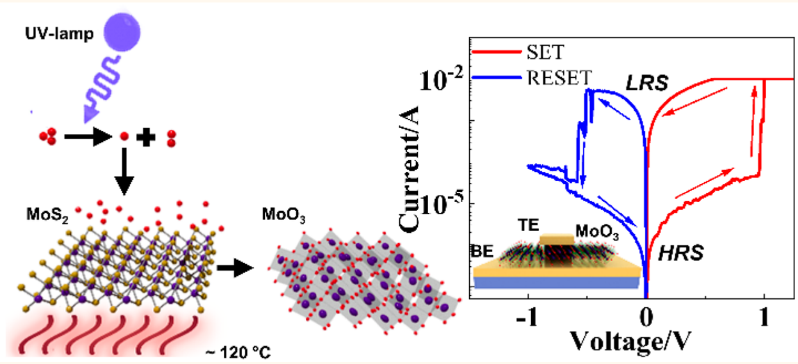

ABSTRACT: **Molybdenum trioxide (MoO_3), an important transition metal oxide (TMO), has been extensively investigated over the past few decades due to its potential in existing and emerging technologies, including catalysis, energy and data storage, electrochromic devices, and sensors. Recently, the growing interest in two-dimensional (2D) materials, often rich in interesting properties and functionalities compared to their bulk counterparts, has led to the investigation of 2D MoO_3. However, the realization of large-area true 2D (single to few atom layers thick) MoO_3 is yet to be achieved. Here, we demonstrate a facile route to obtain wafer-scale monolayer amorphous MoO_3 using 2D MoS_2 as a starting material, followed by UV−ozone oxidation at a substrate temperature as low as 120 °C. This simple yet effective process yields smooth, continuous, uniform, and stable monolayer oxide with wafer-scale homogeneity, as confirmed by several characterization techniques, including atomic force microscopy, numerous spectroscopy methods, and scanning transmission electron microscopy. Furthermore, using the subnanometer MoO_3 as the active layer sandwiched between two metal electrodes, we demonstrate the thinnest oxide-based nonvolatile resistive switching memory with a low voltage operation and a high ON/OFF ratio. These results (potentially extendable to other TMOs) will enable further exploration of subnanometer stoichiometric MoO_3, extending the frontiers of ultrathin flexible oxide materials and devices.**

KEYWORDS: *wafer-scale, monolayer, molybdenum oxide, amorphous, resistive switching memory*

INTRODUCTION

Molybdenum trioxide (MoO_3), particularly the α-MoO_3 phase, has attracted significant attention due to its thermodynamic stability and layered structure,[1,2] together with interesting electronic,[3−5] optical,[6] catalytic,[7] and electrochemical[8] properties. Notably, stoichiometric α-MoO_3 is a semiconductor with a large electron affinity (>6 eV), wide bandgap (>3 eV), and high ionization energy (>9 eV).[9,10] As a result, many applications, including catalysis,[11] sensors,[12,13] organic light-emitting diodes (OLEDs),[14] batteries,[15] memory,[3,4] and electrochromic devices,[16,17] have been successfully demonstrated by engineering these interesting properties. Bulk MoO_3 in the orthorhombic phase (α-MoO_3) is made of atomically

Received: September 2, 2021
Accepted: February 14, 2022
Published: February 21, 2022

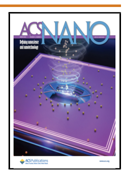

https://doi.org/10.1021/acsnano.1c07705
ACS Nano 2022, 16, 3756–3767

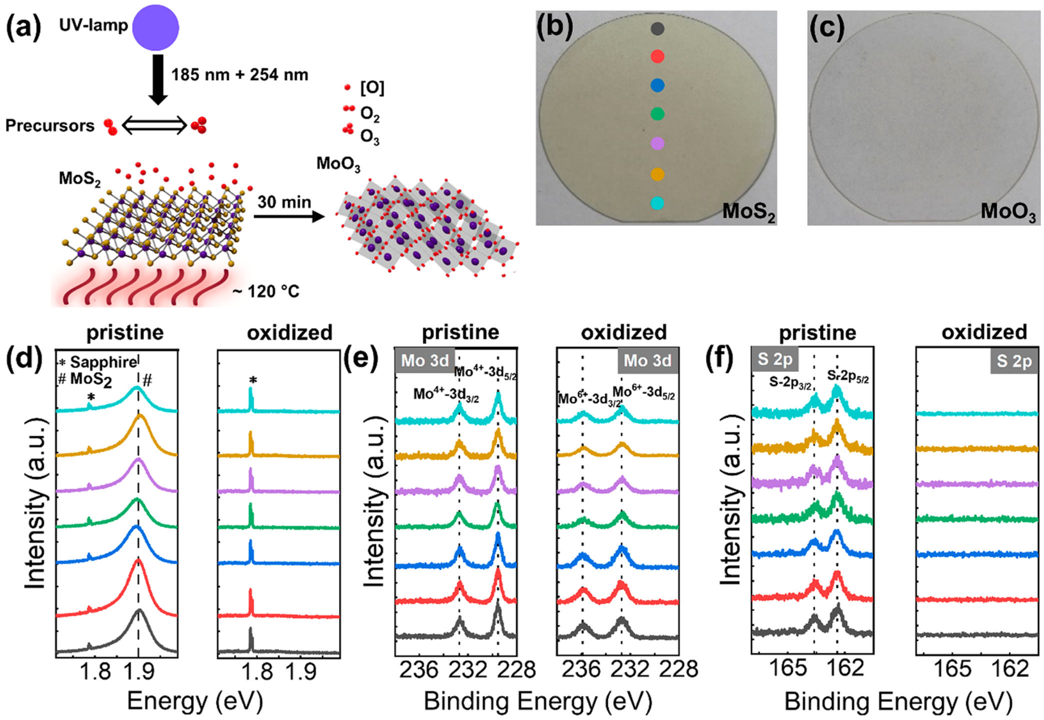

Figure 1. UV−ozone oxidation of wafer-scale MoS_2. (a) Under the UV light, ambient oxygen converts into ozone (ozone generation) and the generated ozone reverts (ozone decomposition) to ambient oxygen. Atomic oxygen is produced during ozone generation and decomposition, which reacts with MoS_2 and converts it to MoO_3. Two inch sapphire wafer with MOCVD grown monolayer MoS_2 (b) before and (c) after 30 min of UV−ozone oxidation at 120 °C. The 2D MoS_2 converts into a transparent film after oxidation. (d) Photoluminescence spectra on the marked locations (color-coded accordingly in b) of the wafer. The distinct sharp peak at 1.9 eV characteristic of monolayer MoS_2 disappears after oxidation. The peak at ∼1.78 eV corresponds to the underlying sapphire substrate. High-resolution XPS spectra on the marked locations for (e) Mo 3d and (f) S 2p peaks.

thin sheets (≈0.7 nm), with each sheet consisting of double layers of linked and distorted MoO_6 octahedra.[18] The double-layers are stacked with weak out-of-plane van der Waals (vdW) forces with strong in-plane covalent bonding.

Two-dimensional (2D) MoO_3, often different in physical and chemical properties compared to the bulk counterpart,[19] is highly desired for integrating with other 2D materials. Despite the rich physical phenomena and potential technological benefits, the material synthesis has not yet matured enough to produce controlled and repeatable growth of large-area, uniform, and high-quality 2D MoO_3. Like other 2D materials, the best quality 2D oxides are usually obtained from the mechanical exfoliation of bulk crystals.[20,21] However, this lab standard top-down approach is not technologically scalable in its current form due to the random nature, low yield, and inadequate area coverage. More extensive area coverage can be obtained through liquid exfoliation, an ultrasonication-assisted or ion-intercalation-based exfoliation method suitable for producing large-area thin film.[12,22] Yet the monolayer yield is poor (no more than a few tens of percent by number), impeding the immediate translation into technological applications.[23] Liquid phase deposition, such as electro-deposition,[16] hydrothermal,[24] and sol−gel,[25] was studied too, primarily producing bulk materials with small domains.

Vapor phase synthesis, especially physical vapor deposition (PVD), has been a well-known method for scalable and repeatable synthesis, offering good crystalline film with controlled stoichiometry and morphology. Among various PVD methods, thermal evaporation has been widespread for the synthesis of α-MoO_3 for the ease of control over the deposition parameters, with reports of large-area thin films in the temperature range 400−600 °C.[26−28] Ultrathin materials, even down to a few atomic layers, have been reported with vdW epitaxy.[29,30] Molecular beam epitaxy (MBE) has been explored to realize atomically thin films, but the crystal size is limited to only a few micrometers.[31,32] Pulsed laser deposition (PLD)[33] and atomic layer deposition (ALD)[34] have also been exercised successfully. In addition, chemical vapor deposition (CVD), another vapor phase technique, has been successfully applied in the synthesis of MoO_3 thin films.[3,17] However, none of these methods mentioned above could produce a single-layer film of an area larger than few tens of micrometers. Moreover, the precise control over the lateral (size) and vertical (thickness) dimension of the film with a uniform atomically thin layer is yet to be achieved with these methods. In addition, the comparatively high temperature and relatively long process pose additional material integration challenges for technologically relevant applications.

Recently, the transport, electronic, and optoelectronic properties of 2D MoS_2 have been modified by various surface functionalization techniques, including thermal,[35−37] oxygen-plasma,[38−43] and UV−ozone oxidation.[44−47] Some of these functionalization techniques can lead to the complete/partial conversion of the topmost 2D MoS_2 layer(s) into 2D surface oxides, yielding stoichiometric MoO_3 after careful process optimization. There have been few reports of such atomic layer conversion of 2D MoS_2 into 2D MoO_3 with a very limited characterization of the oxide.[39,42,43,47,48] As such, a detailed and comprehensive study of the 2D monolayer MoO_3 has yet

https://doi.org/10.1021/acsnano.1c07705
ACS Nano 2022, 16, 3756−3767

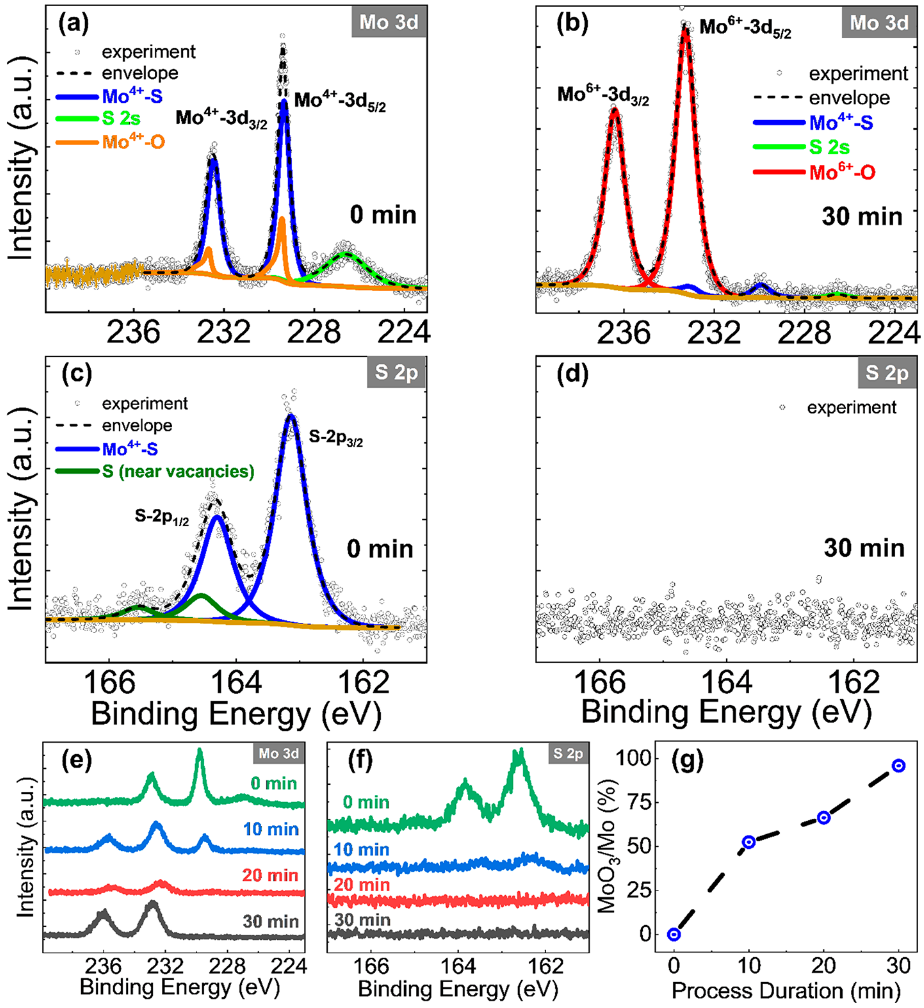

Figure 2. High-resolution XPS spectra of monolayer MoS_2. Mo 3d core-level peaks of (a) pristine MoS_2 and (b) MoS_2 following 30 min oxidation at 120 °C. S 2p core-level peaks of (c) pristine MoS_2 and (d) MoS_2 following 30 min oxidation at 120 °C. Comparison of (e) Mo 3d and (f) S 2p core level peaks oxidized for various durations. (g) Conversion of Mo into MoO_3 with respect to the processing time. As the process duration increases, the extent of oxidized Mo (MoO_3) increases. For a process duration of 30 min, approximately 96% of Mo gets oxidized and turned into MoO_3.

to be conducted. Moreover, no report of large-area single-layer MoO_3 has been reported to the best of our knowledge.

In this work, we report the demonstration of UV−ozone-based conversion (a gentle oxidation process suitable for preserving material integrity) of 2D MoS_2 crystals into 2D amorphous MoO_3 in a layer-by-layer precision. This low-temperature (∼120 °C) and straightforward (process time ∼30 min) conversion method is also scalable to a whole wafer, as demonstrated by converting a 2 in. homogeneous polycrystalline single-layer MoS_2 into a uniform and continuous amorphous monolayer MoO_3. A systematic study was performed to investigate the structural, chemical, optical, and electrical properties of the monolayer film by using a combination of various spectroscopic and microscopic techniques, including cathodoluminescence (CL) spectroscopy, X-ray photoelectron spectroscopy (XPS), electron energy loss (EEL) spectroscopy, scanning transmission electron microscopy (STEM), and atomic force microscopy (AFM). The XPS study confirms the evolution of Mo^{6+} at the expense of Mo^{4+}, indicating the conversion of 2D MoS_2 into MoO_3, while the nature of the MoO_3 film was found to be amorphous from the annular dark field (ADF)-STEM study. In addition, an atomic level investigation at the film cross-section by spatially resolved EEL spectroscopy shows the hybridization between O 2p and Mo 4d, probably due to the formation of MoO_3. Notably, a homogeneous, ultraflat (roughness ∼0.30 nm), and uniform monolayer film (thickness ∼0.70 nm) with a bandgap of ∼3.1 eV was formed, as confirmed from the Raman mapping, AFM scans, and CL measurements. Subsequently, memristor devices were fabricated on the atomically thin MoO_3 film, and a nonvolatile resistive switching phenomenon was observed. This thinnest memory device also offers low-voltage operation (<1 V), a high ON/OFF ratio (>10^7), and forming-free switching, all desirable for energy-efficient storage and neuromorphic computing.

RESULTS AND DISCUSSION

Figure 1a shows the process of UV−ozone oxidation by using a benchtop UV cleaner. Under UV light (185 and 254 nm wavelength) illumination, ozone generation and decomposition (see the Methods section and Figure S1 for more details) occur, as expressed by the following equations:[49]

Ozone generation (<200 nm):

$$O_2 \rightarrow O + O \quad (1)$$

$$O + O_2 \rightarrow O_3 \quad (2)$$

Ozone decomposition (200−300 nm):

$$O_3 \rightarrow O + O_2 \quad (3)$$

Atomic oxygen, a strong oxidizing agent, is created during ozone generation and decomposition. That, in turn, oxidizes the MoS_2 into MoO_3, as shown in the following equation:[49]

Oxidation:

$$2MoS_2 + 7O_2 \rightarrow 2MoO_3 + 4SO_2 \quad (4)$$

The total enthalpy change of the above reaction is estimated to be −2347 kJ/mol.[50,51] The experimental setup includes a benchtop UV cleaner (PSD Thermal Series UV−ozone Cleaner from Novascan) containing a PID controlled heating stage (4 in. × 4 in.) and a low-pressure mercury lamp (Figure S1). The sample is mounted on the stage and heated at 120 °C while the UV light is ON. Figure 1b shows an optical micrograph of a wafer-scale MOCVD-grown MoS_2 (the details of growth can be found in the Methods section) on a 2 in. sapphire substrate.[52,53] Raman spectroscopic analysis revealed the in-plane E^1_{2g} and out-of-plane A_{1g} characteristics peaks at ∼388 and ∼406 cm^{-1} (separation ∼18 cm^{-1}, typical to monolayer MoS_2), as shown in Figure S2. Full-width at half-maximum (fwhm) of E^1_{2g} and A_{1g} are <4 and <7 cm^{-1}, respectively, suggesting the good crystalline quality of the film. Figure S2 compares Raman spectra from seven marked locations on the wafer shown in Figure 1b. The negligible variation in the peak position and intensity reveals the uniformity of the grown material. The homogeneity of the film is reconfirmed by the Raman maps (Figure S3) and AFM images (Figure S4) acquired from different locations across the wafer. Following oxidation at 120 °C for 30 min, the MoS_2 film on sapphire transforms into a transparent film, as seen in Figure 1c. Raman spectroscopic analyses at the marked locations now show no detectable peaks characteristic to MoS_2, indicating a complete conversion of MoS_2 film (Figure S2). Similarly, the sharp, distinct peaks at 1.9 eV (fwhm <0.06 eV) from PL spectroscopies, characteristic to pristine monolayer MoS_2, at the marked locations disappear upon oxidation (Figure 1d). The doublet at ∼1.78 eV corresponds to the characteristic peak of the underlying sapphire substrate. To investigate the effect of UV−ozone oxidation on MoS_2, the elemental compositions of the pristine and oxidized films were analyzed by XPS measurements. The XPS survey spectra are shown in Figure S5. Figure 1e shows the high-resolution XPS spectra of Mo 3d peaks at the marked locations. The binding energies of Mo $3d_{5/2}$ and Mo $3d_{3/2}$ at ∼229.5 and ∼232.7 eV correspond to the +4 oxidation state of Mo as previously seen in the case of MoS_2.[54,55] Following oxidation, the Mo peaks shift to higher binding energies of 232.7 and 235.9 eV showing conversion to a Mo^{6+} oxidation state. More detailed analysis and quantification are discussed in Figure 2. High-resolution XPS spectra for S 2p peaks are shown in Figure 1f. After oxidation, the absence of S 2p peaks corroborates that all the MoS_2 has been converted to molybdenum oxide (Figure 1f).

To identify the nature of oxides and study the effect of oxidation duration on the MoS_2 films, elemental analysis and chemical stoichiometry quantification were performed *via* XPS studies. Figure 2 shows the high-resolution XPS spectra for pristine and oxidized MoS_2. In Figure 2a, the binding energies of Mo $3d_{5/2}$ and Mo $3d_{3/2}$ at ∼229.5 and ∼232.7 eV correspond to the +4 oxidation state of Mo, as previously seen in the case of pristine MoS_2.[54,55] Additionally, the as-grown monolayer has a minimal presence of Mo (IV) oxide, as evident from the two peaks appearing at 230.4 and 233.6 eV (Mo^{4+} $3d_{5/2}$ and Mo^{4+} $3d_{3/2}$, respectively). This limited contribution from the Mo (IV) oxide peak may arise due to the exposure to ambient and/or surface adsorbed oxygen, as seen previously in the case of CVD-grown MoS_2.[56] The complete absence of any photoelectron peak at 236−236.5 eV (Figure S6), where the characteristic Mo $3d_{3/2}$ peak for Mo (V) and Mo (VI) atoms are detected, confirms that the as-grown film does not contain Mo in a higher oxidation state than (IV). To demonstrate the gradual oxidation of the film with increasing exposure duration, Figure 2e shows the high-resolution XPS analyses of the samples with varying exposure times such as 0, 10, 20, and 30 min. Oxidation of the as-grown monolayer MoS_2 film by exposure to UV−ozone at 120 °C for 10 min converts all of the Mo (IV) oxide as well as significant amounts of Mo (IV) sulfide to Mo (VI) oxide. This is demonstrated in Figure S7 by the disappearance of the Mo (IV) oxide peaks at 230.4 and 233.6 eV (clearly visible in Figure 2a) and the emergence of a new doublet at 233.2 and 236.3 eV that corresponds to Mo^{6+} $3d_{5/2}$ and Mo^{6+} $3d_{3/2}$, respectively.[57,58] Small amounts of nonstoichiometric Mo (V) oxides can also be observed at 232.1 and 236.3 eV, corresponding to Mo^{5+} $3d_{5/2}$ and Mo^{5+} $3d_{3/2}$, respectively (Figure S7). After an oxidation duration of 20 min, the Mo^{6+} peaks almost doubled in intensity compared to Mo^{4+} peaks, showing a substantial increase in film oxidation, as shown in Figure S7. At 30 min, all MoS_2 is converted to MoO_3, as shown in Figure 2b,e.

Parts c, d, and f of Figure 2 show the corresponding S 2p peaks. The characteristic photoemission peaks at 163.1 eV (S $2p_{3/2}$) and 164.3 eV (S $2p_{1/2}$) correspond to the −2 oxidation state of sulfur in as-grown MoS_2 (Figure 2c).[59] A small additional doublet (Figure 2c) characteristic of sulfur atoms near vacancies is also detected in the S 2p region, thus indicating the ejection of sulfur from the film and suggesting the formation of substoichiometric MoS_2.[60] The quantification of the Mo/S ratio using either the S 2p signal or the S 2s signals (Figure 2c), which was computed to be 1:1.9, confirms the presence of a nonstoichiometric sulfide, whose origin may be attributed to the presence of oxides and/or sulfur (S) vacancies in the CVD grown film. With increasing oxidation duration, the S-content of the film gradually reduces, as seen from the diminishing S 2p peaks in Figure 2f. The presence of a SO_x doublet at 168.5−169 eV in the S 2p region for the film oxidized for 10 min indicates that at least some of these nonstoichiometric Mo (V) states are oxi-sulfide intermediates, as shown in Figure S7.[61,62] For a sulfurization duration of 30 min, the intensity of the S 2p peaks is below the detection limit (Figure 2d,f), confirming the absence of any MoS_2 in the remaining film. The change in MoO_3/Mo peak areas with increasing oxidation duration is shown in Figure 2g, demonstrating the gradual conversion of MoS_2 film to MoO_3 with negligible intermediate oxides (<5%). The percentage of suboxides can be found in Figure S8. Finally, we have also added O 1s spectra in Figure S9.

Next, ADF-STEM was performed on oxidized monolayer (with few secondary domains) 2D MoS_2 crystals (CVD grown) to obtain an atomic-scale insight into the conversion process and the outcome. The process was intentionally stopped after 15 min (as opposed to the routine time of 30 min) to avoid the complete conversion of the 2D MoS_2 crystal.

https://doi.org/10.1021/acsnano.1c07705
ACS Nano 2022, 16, 3756−3767

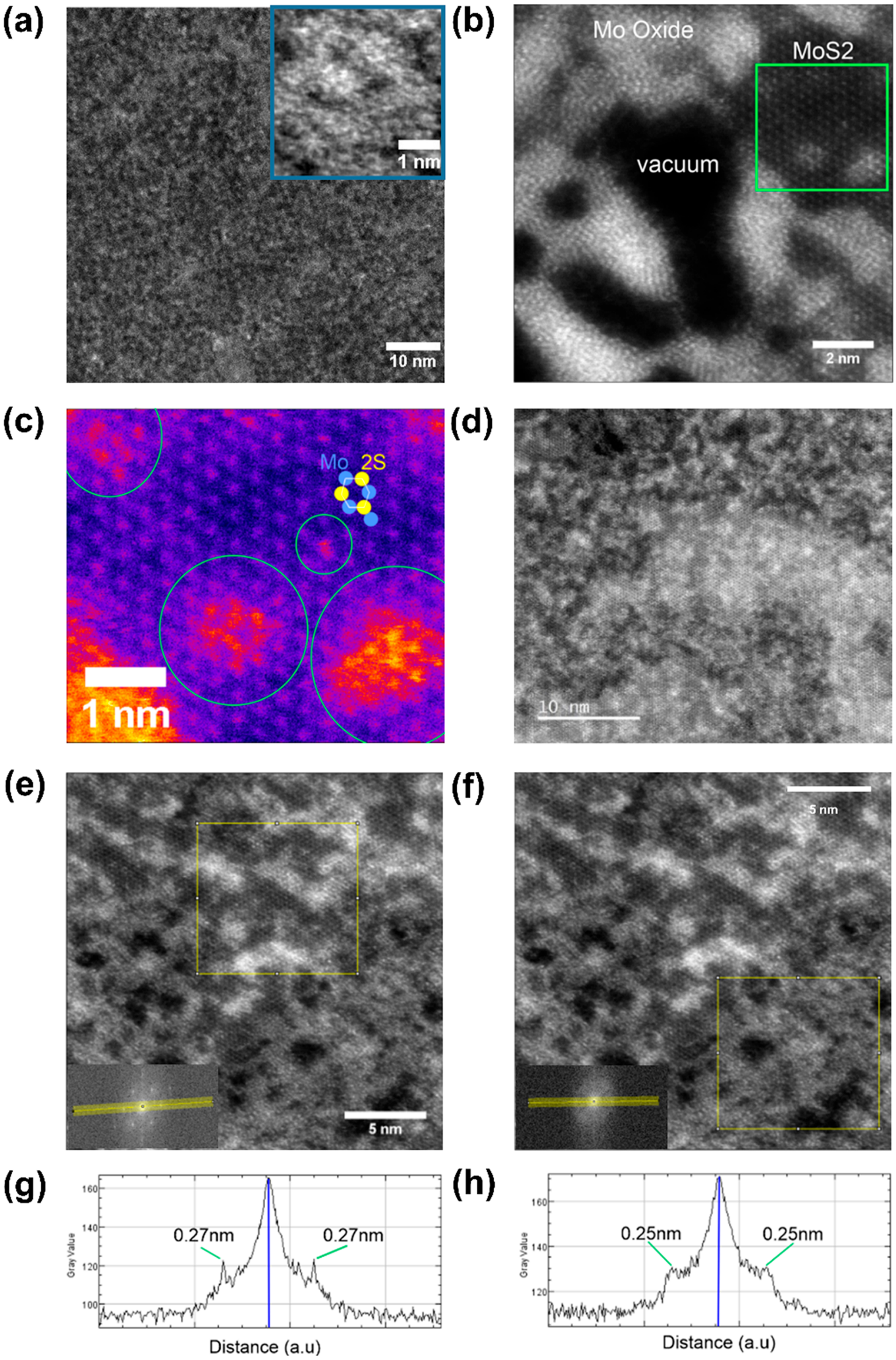

Figure 3. ADF-STEM characterization of UV−ozone oxidized CVD MoS_2 at room temperature. (a) ADF-STEM image of oxidized MoS_2. Inset, high-magnification ADF-STEM image of the amorphous material. (b) ADF-STEM image of a region of MoS_2, amorphous oxide, and vacuum (void). (c) Magnified view of the green box area in (a) showing the MoS_2 lattice and surface oxide reactions (green ovals). (d) ADF-STEM image of a bilayer region of MoS_2. (e) ADF-STEM image showing the crystalline MoS_2 region. Inset (bottom left), the power spectrum from the yellow box in (e) is calculated by the FFT. (f) ADF-STEM image showing the amorphous region. Inset (bottom left), the power spectrum from the yellow box region in (f) is calculated by the FFT. (g) Line profile is taken from the yellow region in (e). (h) Line profile is taken from the yellow region in (f).

https://doi.org/10.1021/acsnano.1c07705
ACS Nano 2022, 16, 3756−3767

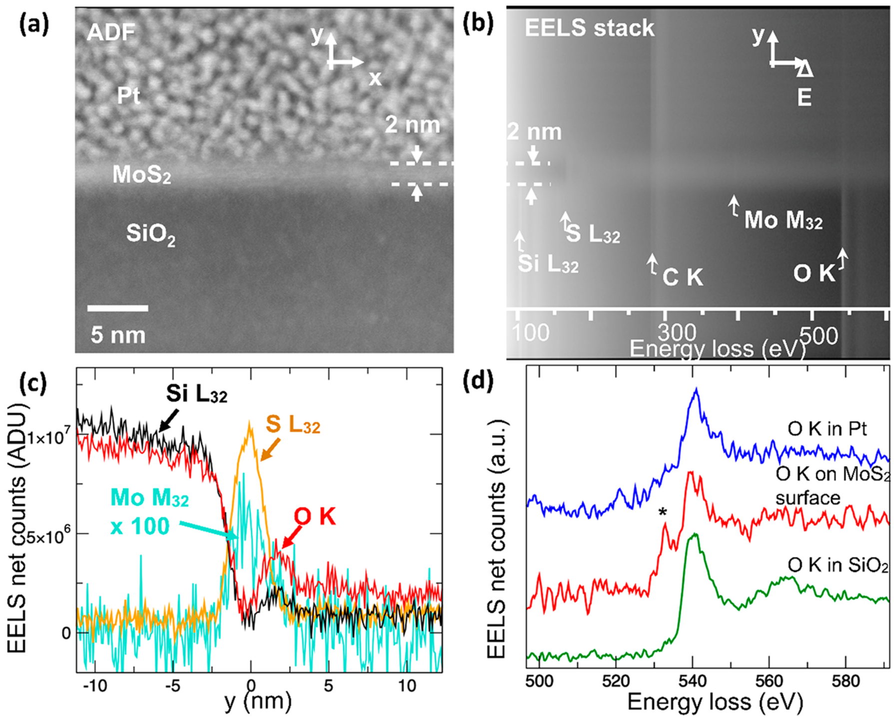

Figure 4. Spatially resolved electron energy loss (EEL) spectroscopy. EEL measurements were done with the StripeSTEM method,[66] by which spectra are collected simultaneously with an image scan. (a) ADF image showing a triple-layer MoS_2 layer sandwiched between the SiO_2 support and Pt protective layer. (b) EEL spectra taken line-by-line in parallel with the image scan. Each line in the stack image displays the EEL intensity cumulated over a scan line in the image. Markers indicate the onset of elemental core loss excitations for Si, S, Mo, and O. (c) Intensity profiles extracted from the EEL spectra after background subtraction as a function of the coordinate orthogonal to the MoS_2 layer stack. The signal intensity in each profile is related to the elemental concentration. The oxygen signal shows a pronounced peak on the top surface of the MoS_2. (d) Fine structure of the O−K edge in three different locations: in the SiO_2 support, on the top surface of the MoS_2, and in the protective Pt layer. The O−K pre-edge feature (marked by an asterisk) in the spectrum extracted from the top surface of the MoS_2 indicates a hybridization between O 2p and Mo 4d states.

Figure 3 shows an ADF-STEM image of the area of oxidized MoS_2 that is amorphous. The region shows a relatively uniform thickness in the long-range (10−100 nm) but with some nanoscale porosity in the sub 10 nm scale (inset). The oxidized MoS_2 film is supported by an amorphous carbon layer beneath. The amorphous carbon has weak scattering and barely contributes contrast to the ADF-STEM image relative to the heavier Mo-based materials. Figure 3b shows a region where some of the monolayer MoS_2 is still intact, next to the amorphous oxide region. The number density of Mo in a single-layer crystalline α-MoO_3 is roughly 18% higher than 1L MoS_2.[42,63,64] As such, in principle, the 2D conversion would create voids (nanoscale) unless there is a significant mass transport to compensate the lattice parameter differences. We have also observed the voids/vacuum in Figure 3b due to the nanoporosity of the oxide material. However, as Raman, PL, and AFM experiments confirmed, no voids or discontinuity are observed on the microscopic scale. Figure 3c shows the region from the green box in Figure 3b. The excessive Mo atoms are seen on the MoS_2 with increased contrast in the regions indicated by the green ovals. These regions indicate MoS_2 that has begun oxidation and the start of the phase transformation from monolayer MoS_2 into the ultrathin MoO_3 material. Some regions of the sample still contained a MoS_2 bilayer lattice (outside the green oval) structure, as seen in the central area of Figure 3d, where the 2H stacked region is visible. The rest of the surrounding area still contains lattice from the MoS_2 but the surface is coated with an amorphous Mo oxide layer. This shows that only the top layer is oxidized during the reactions and that the underlying bottom layer remains relatively intact and retains its MoS_2 lattice structure. This is examined in more detail in Figure S10. Parts e−h of Figure 3 examine the reciprocal space features of the MoS_2 and oxide regions. In Figure 3e, a region of monolayer MoS_2 is still present, and the power spectrum calculated by the fast Fourier transform (FFT) (inset of Figure 3e) shows sharp spots in its reflections, indicative of its crystallinity. A line profile taken across the inset of Figure 3e is shown in Figure 3g, and the MoS_2 lattice peaks (0.27 nm) are clearly seen. In Figure 3f, the amorphous region is selected, and the power spectrum is shown in the inset. No sharp spots or reflections are observed. A line profile across the inset of Figure 3f reveals weak broad peaks at 0.25 nm (Figure 3h), which measures the average lateral spacing of the amorphous material in the X−Y plane.

In order to roughly estimate the thickness of the amorphous material, we found a region of crystalline MoS_2 monolayer and used this as a reference guide (Figure S11). Several line profiles were taken to measure regions of MoS_2, Mo−O amorphous material, and vacuum. The signal from the amorphous regions was slightly higher in intensity relative to MoS_2. Vacuum regions gave counts of ∼6×10^5, MoS_2 had counts of $8-9 \times 10^6$, and Mo−O regions had counts of $9-10 \times 10^6$. This provides good evidence that the oxidation process leads to an ultrathin amorphous material similar in thickness to its original starting material of MoS_2. Direct measurement of the step height on the edge of an oxidized MoS_2 (single-crystal CVD MoS_2 oxidized by the same recipe) by AFM leads to a thickness of ∼0.7 nm (Figure S12), consistent with the

https://doi.org/10.1021/acsnano.1c07705
ACS Nano 2022, 16, 3756−3767

reported data for monolayer oxides.[65] The baseline-corrected cathodoluminescence (CL) spectroscopy performed on this single-layer amorphous MoO_3 shows a peak position around 3.1 eV, as shown in Figure S13, suggesting an optical bandgap value ~3.1 eV consistent with the reported data for amorphous MoO_3.[42]

To obtain the atomic resolution profile of the MoO_3, spatially resolved EEL spectroscopy was performed in a STEM. The TEM sample was prepared by oxidizing a four-layer (4L) MoS_2 (exfoliated on SiO_2/Si substrate) under the same conditions mentioned above for 15 min to oxidize the topmost layer. This process led to the top layer's oxidation with the bottom three layers not oxidized, forming a MoO_3/MoS_2 (1L/3L) heterojunction, where the layer number was confirmed from Raman spectroscopy (Figure S14). Cross-section TEM samples were prepared by lamellae cut in a focused ion beam (FIB) instrument out of this MoO_3 (1L)/MoS_2 (3L)/SiO_2/Si structure. Before FIB milling, a protective layer of platinum (Pt) was deposited on top of the MoO_3 film (see more details in the Methods section). Figure 4a shows an ADF image of 3L MoS_2 (~2 nm) sandwiched between SiO_2 support and the Pt protective layer. EEL spectra were taken line-by-line in parallel with the image scan, as shown in Figure 4b. Each line in the stack image of EEL spectra displays the energy loss intensity accumulated over a scan line in the image. Markers indicate the onset of elemental core loss excitations for Si, S, Mo, and O. We also note the presence of carbon signal, possibly from sample contamination under observation. To retrieve the elemental profiles of Si, S, Mo, and O, the corresponding intensity profile was extracted after background subtraction, with the background-subtracted signal integrated over a window of a few 10 eV above the onset of the absorption edge. The intensity profile (related to concentration of the elements) as a function of the coordinate normal to the MoS_2 surface is shown in Figure 4c. The oxygen signal shows a pronounced peak at the interface of MoS_2 and Pt. Otherwise, the Si and O signals are mostly coincident in SiO_2 and MoS_2 regions. Residual O and parasitic Si are observed in the Pt capping layer, a sign of surface damage during FIB milling. Notably, the O peak at the MoS_2/Pt interface starts before the onset of the parasitic Si peak. The fine structure of the O−K absorption edge in SiO_2, MoS_2 surface, and Pt is shown in Figure 4d for further information on the bonding. The O−K fine structure obtained from the MoS_2 surface is distinctive from that of SiO_2, with a pre-edge feature observed in the former. The pre-edge feature (marked by an asterisk) in the spectrum extracted from the top surface of the MoS_2 indicates a hybridization between O 2p and Mo 4d states, suggesting the presence of MoO_3 at the interface.

Transition metal oxides (TMOs) have been widely used as the active layer in resistive switching-based nonvolatile memory (NVM) devices.[67−69] The nonvolatile resistance switching (NVRS) devices store information by switching between a high-resistance state (HRS) and a low-resistance state (LRS), where the state can sustain without a power supply. The MoO_3 obtained from the oxidation of monolayer MoS_2 has been used in the NVRS device, allowing for a subnanometer thick active layer that is otherwise difficult to obtain with conventional metal-oxide-based devices. Two different types of NVRS devices, such as (i) the crossbar devices (Figure S15) and (ii) the litho-free devices (Figure 5), are fabricated and characterized. The crossbar devices can offer a smaller active device area where the active layer (MoO_3) is

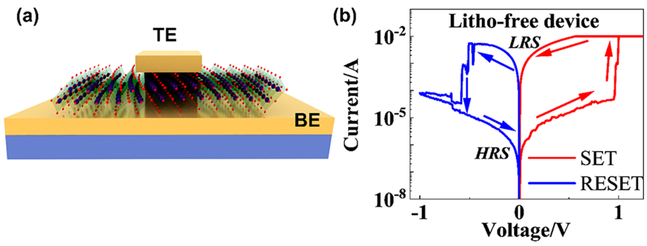

Figure 5. Nonvolatile resistive switching (NVRS) memory based on monolayer MoO_3. (a) Schematic and (b) representative $I-V$ curve of the litho-free device. Top electrode area is 15 × 15 μm^2.

sandwiched between the local bottom electrode (BE) and the top electrode (TE). The electrodes (Cr/Au 2/60 nm) are patterned by e-beam lithography, subsequent e-beam metal deposition, and metal lift-off. The channel material is transferred on BE by using a PDMS-based transfer method. A representative $I-V$ switching curve for a MoO_3 crossbar device is shown in Figure S15. The device starts at HRS. With a voltage sweeping to ~3.2 V, the current abruptly increases to the compliance (1 mA), indicating a transition from HRS to LRS (SET process). To RESET the device from LRS back to HRS, a reverse bias is needed in a bipolar operation (the current decreases at ~ −0.5 V). On the contrary, the litho-free devices have active channel material between ultraflat Au-film BE and local TE. The ultraflat metal film is deposited on a silicon substrate where large-area MoS_2 can be exfoliated and subsequently converted into MoO_3 by UV−ozone oxidation described above. Later, local top electrodes are obtained by e-beam metal deposition with a shadow mask, making the whole device fabrication a litho-free process, thereby offering process contamination and residue-free interfaces. The switching behavior (Figure 5b) with low switching voltages at ~1 V for SET and ~ −0.5 V for RESET confirms that the observed NVRS phenomenon is an intrinsic property for MoO_3. Note that the forming process is not needed in these devices, an initial step before the switching cycles required to establish a conductive filament in most bulk metal-oxide-based NVRS devices. The demonstration of the subnanometer MoO_3-based NVRS devices not only set a record for the thinnest oxide-based resistive switching phenomenon but also inspires further applications on ultrathin flexible nonvolatile memory fabrics and neuromorphic computing with the advantages of a small switching voltage (<1 V), large ON/OFF ratio (>10^7), and forming-free characteristics.

Finally, we have compiled a list of relevant conversion methods for obtaining atomically thin MoO_3, as shown in Table 1. Another list comparing various synthesis methods can be found in Table S1. Moreover, a detailed comparison among UV−ozone, thermal, and oxygen-plasma methods has been conducted in Figure S16.

CONCLUSIONS

In summary, we developed a simple and repeatable method of obtaining wafer-scale subnanometer amorphous stoichiometric MoO_3 by UV−ozone oxidation of MoS_2. Raman/PL, AFM, and XPS confirmed a highly uniform, continuous, and homogeneous film, evidenced by nearly identical data from spatially different regions across the wafer. The film was amorphous, as demonstrated by the absence of a long-range order in the atomic resolution STEM images. In addition, more than 95% of the starting 2D MoS_2 crystal converted into

https://doi.org/10.1021/acsnano.1c07705
ACS Nano 2022, 16, 3756−3767

Table 1. Different Methods for Conversion of Mono- and Few-Layer MoS_2 into MoO_3

oxidation method	lateral size	minimum thickness (nm)	limitations	references
UV−ozone	wafer-scale	0.7		this work
UV−ozone	100−200 μm	0.7	structure damaged	70
UV−ozone	∼10−20 μm	0.7	rough surface	45
UV−ozone	∼1 cm	0.7	rough surface suboxides present	47
oxygen−plasma	<100 μm	1.8	suboxides present rough surface	41 and 42
thermal	∼10−20 μm	0.7	>400 °C etch pits (nonuniform)	35 and 36

a stoichiometric 2D MoO_3, as estimated from the XPS analysis. Spatially resolved EEL spectra taken in a cross-sectional geometry show the hybridization between O 2p and Mo 4d, possibly originating from the presence of interfacial MoO_3. Single-layer oxide (<1 nm) was used as the active layer in a resistive switching-based forming-free NVRS memory device, representing the thinnest oxide-based resistive switching layer. This method of conversion is potentially extendable for other TMDs to realize TMOs with varying transition metals.

METHODS

UV−Ozone Oxidation. A benchtop UV cleaner (PSD Thermal Series UV−Ozone Cleaner from Novascan) with a PID controlled heating stage (4 in. × 4 in.) was used for the oxidation. The UV light is a low-pressure mercury lamp (generates light with 184.9 and 253.7 nm wavelengths) placed about 13 cm from the heating stage. The wavelength of 184.9 nm (typically <200 nm) strikes molecular oxygen in the system and splits the molecule into two single oxygen atoms known as atomic oxygens. The freed oxygen atom then combines with molecular oxygen to form an ozone molecule called ozone generation.

Conversely, the molecular ozone is struck by the ray of 253.7 nm (typically 200−300 nm) and dissociated into molecular and atomic oxygen, a process called ozone decomposition. Thus, atomic oxygen, a strong oxidizing agent, is created in the process of both ozone generation and decomposition. To further enhance the process, this UV−ozone cleaner has a heating stage (maximum temperature 150 °C) to elevate the energy state of the sample surface and drive off the humidity layers that may block oxidation. The topmost layer is oxidized after an oxidation time of ∼10 min, while it takes >15 min for oxidation of the top two layers (Figures S17−S19). After that, the oxidation terminates itself due to the diffusion barrier of incoming atomic oxygen through it. As such, the process can be called a self-limiting process.

2D Materials Preparation and Characterization. MOCVD grown wafer-scale MoS_2 was achieved in a single step process at 1000 °C, with molybdenum hexacarbonyl ($Mo(CO)_6$) as a metal precursor and hydrogen sulfide (H_2S) as the chalcogen source with H_2 as the carrier gas.[52,53] The coalesced monolayer growth across the 2 in. wafer was achieved in 18 min. The substrate was cooled in H_2S to 300 °C to inhibit decomposition of the film after the growth is achieved. Optical characterization was performed using an Olympus microscope (BX53M) and their proprietary software Stream Essentials. Raman spectroscopy was performed in a Renishaw inVia micro-Raman system. An excitation wavelength of 532 nm with an incident beam power of ∼1 mW and an exposure time of 10 s were used for Raman. A 3000 l/mm grating was used for <5 cm^{-1} resolution. The CL was performed in an SEM (JEOL JSM-6500F) with a Gatan MonoCL3 system under an accelerating voltage of 5 kV at room temperature. A region of interest with a size of 15 × 20 μm^2 was selected and scanned under fast scan mode. The emitted light was collected under a step size of 1 nm and a dwell time of 2 s.

XPS Characterization. XPS spectra (Omicron Multiprobe system with base pressure below 3 × 10^{-10} mbar) were acquired using monochromatic Al−Kα (hυ = 1486.7 eV) operated at 15 kV at room temperature. The photoelectrons were collected with an emission angle (EA) of 42.5°. XPS spectra were obtained with an incident X-ray beam of 6.3 mm diameter. For high-resolution spectra, the measurements were performed in constant-analyzer-energy (CAE) mode with a pass energy of 10 eV and a step size of 0.01 eV (fwhm of the peak for Ag $3d_{5/2}$ is 0.60 eV). Survey spectra were collected using a pass energy of 100 eV and a step size of 1 eV. The high-resolution spectra were processed using CasaXPS (v2.3.16, Casa Software Ltd.). Peak fitting was performed after background subtraction, which was carried out using an iterated Shirley−Sherwood algorithm. The peak binding energies were referred to the aliphatic carbon signal at 284.7 eV. Quantitative analysis of XPS data was performed using the method described in ref 71. Briefly, once the integrated area was obtained from fitting the original spectra after background subtraction, the quantification was performed using the first principle with Powell's equations.[72] The inelastic mean free path was computed using the TPP-2 M formula.[73] The lineshapes for the synthetic peaks used to fit the experimental data were determined through the analysis of reference compounds, namely, MoS_2, MoO_2, and MoO_3.

STEM Characterization. ADF-STEM experiment was conducted using JEOL ARM-300CF, equipped with a JEOL ETA corrector at the electron Physical Sciences Imaging Centre (ePSIC) at Diamond Light Source. The imaging was carried out at the accelerating voltage of 60 kV. A dwell time of 10−20 μs was used for imaging with a pixel size of 0.006 nm px^{-1}, beam current of 48.5 pA, convergence semiangle of 39.1 mrad, and acquisition angles of 56.4−207.1 mrad (inner-outer).

Electron Energy Loss Characterization. STEM images and EEL spectrum data were recorded in a double aberration-corrected Themis-Z transmission electron microscope (Thermo Fisher Scientific Microscopy Solutions, Hillsboro, OR) equipped with a Schottky type high-brightness electron gun and CEOS double hexapole aberration correctors. Measurements were performed at an acceleration voltage of 80 kV to limit radiation damage. Annular dark-field (ADF) images were recorded with a semiconvergence angle of 30 mrad and a probe current of 50 pA, resulting in a probe size of approximately 1.2 Å on a Fischione Model 3000 detector with a collection angle of 80−300 mrad. EEL spectra were recorded on a Gatan Quantum GIF 966ERS energy loss spectrometer (Gatan Inc., Pleasanton, CA) with an Ultrascan1000 CCD camera with a STEM probe with a semiconvergence angle of 30 mrad and a beam current of 80−100 pA. The outer semicollection angle of the spectrometer was 60 mrad.

Energy loss measurements were performed using the StripeSTEM method,[66] by which EEL spectra were collected simultaneously with an image scan. The EEL spectrometer is too slow to resolve a single fast scan line ("*x*-direction") but retains the sampling in the slow scan direction ("*y*-direction"). Aligning an interface normal along the slow scan direction allows for mapping the elemental composition across the interface. The electron dose distribution along scan lines further reduces radiation damage to the sample during the recording of energy loss signals.[74]

Device Fabrication.

- Crossbar: Bottom electrodes (BEs) were patterned by e-beam lithography and deposited with 2 nm Cr/80 nm Au by e-beam

https://doi.org/10.1021/acsnano.1c07705
ACS Nano 2022, 16, 3756−3767

evaporation on Si/SiO_2 substrate. Then, 1L MoS_2 thin film was transferred onto prefabricated BE using a PMDS water-assisted transfer method.[75] Top electrodes (TEs) were prepared using the same procedure as BE.

- Litho-free device: Centimeter-scale MoS_2 thin film can be obtained by exfoliation of MoS_2 bulk crystal (2D Semiconductor Inc.) on the ultraclean and flat Au thin film on a Si substrate (Platypus Technologies, LLC).[76] The Au surface must be very fresh with less than 10 min air exposure, which is the key to the successful large-area MoS_2 exfoliation. The Au thin film can be used as a global BE. A shadow mask was used to deposit TE to avoid any lithography process.

Electrical Characterization. The DC characteristics of the memory devices were performed using a Cascade Microtech Summit 11000B-AP probe station with an Agilent 4156 semiconductor parameter analyzer under ambient conditions.

ASSOCIATED CONTENT

Supporting Information

The Supporting Information is available free of charge at https://pubs.acs.org/doi/10.1021/acsnano.1c07705.

Figures of experimental setup for UV−ozone oxidation, Raman spectra, Raman maps, AFM images, XPS survey spectra, high-resolution XPS, percentage of suboxides as a function of process duration, ADF-STEM images, power spectrum, image of the spatial distribution, line profiles, line scan profiles, cathodoluminescence spectroscopy, UV−ozone oxidation, schematic and representative $I-V$ curve of a crossbar device, comparison among various conversion methods, and UV−ozone oxidation for various time durations, discussions of determination of the O/Mo ratio and evidence for layer-by-layer oxidation control, and table of different methods for synthesis of mono- and few-layer MoO_3 (PDF)

AUTHOR INFORMATION

Corresponding Author

Deji Akinwande − *Microelectronics Research Center, The University of Texas at Austin, Austin, Texas 78758, United States; Texas Material Institute, The University of Texas at Austin, Austin, Texas 78712, United States;* orcid.org/0000-0001-7133-5586; Email: deji@ece.utexas.edu

Authors

Md Hasibul Alam − *Microelectronics Research Center, The University of Texas at Austin, Austin, Texas 78758, United States;* orcid.org/0000-0002-4923-0873

Sayema Chowdhury − *Microelectronics Research Center, The University of Texas at Austin, Austin, Texas 78758, United States;* orcid.org/0000-0001-7670-4846

Anupam Roy − *Microelectronics Research Center, The University of Texas at Austin, Austin, Texas 78758, United States;* orcid.org/0000-0003-1207-0981

Xiaohan Wu − *Microelectronics Research Center, The University of Texas at Austin, Austin, Texas 78758, United States*

Ruijing Ge − *Microelectronics Research Center, The University of Texas at Austin, Austin, Texas 78758, United States;* orcid.org/0000-0002-0768-3057

Michael A. Rodder − *Microelectronics Research Center, The University of Texas at Austin, Austin, Texas 78758, United States*

Jun Chen − *Department of Materials, University of Oxford, Oxford OX1 3PH, United Kingdom*

Yang Lu − *Department of Materials, University of Oxford, Oxford OX1 3PH, United Kingdom*

Chen Stern − *Faculty of Engineering, Bar-Ilan University, IL 52900, Israel; Institute for Nanotechnology and Advanced Materials, Bar-Ilan University, IL 5290002, Israel*

Lothar Houben − *Chemical Research Support, Weizmann Institute of Science, Rehovot, IL 76100, Israel*

Robert Chrostowski − *Texas Material Institute and Materials Science and Engineering Program, The University of Texas at Austin, Austin, Texas 78712, United States*

Scott R. Burlison − *Microelectronics Research Center, The University of Texas at Austin, Austin, Texas 78758, United States*

Sung Jin Yang − *Microelectronics Research Center, The University of Texas at Austin, Austin, Texas 78758, United States*

Martha I. Serna − *Microelectronics Research Center, The University of Texas at Austin, Austin, Texas 78758, United States*

Ananth Dodabalapur − *Microelectronics Research Center, The University of Texas at Austin, Austin, Texas 78758, United States;* orcid.org/0000-0003-4327-8136

Filippo Mangolini − *Texas Material Institute and Walker Department of Mechanical Engineering, The University of Texas at Austin, Austin, Texas 78712, United States;* orcid.org/0000-0003-3360-9122

Doron Naveh − *Faculty of Engineering, Bar-Ilan University, IL 52900, Israel; Institute for Nanotechnology and Advanced Materials, Bar-Ilan University, IL 5290002, Israel;* orcid.org/0000-0003-1091-5661

Jack C. Lee − *Microelectronics Research Center, The University of Texas at Austin, Austin, Texas 78758, United States*

Sanjay K. Banerjee − *Microelectronics Research Center, The University of Texas at Austin, Austin, Texas 78758, United States*

Jamie H. Warner − *Microelectronics Research Center, The University of Texas at Austin, Austin, Texas 78758, United States; Department of Materials, University of Oxford, Oxford OX1 3PH, United Kingdom; Texas Material Institute, The University of Texas at Austin, Austin, Texas 78712, United States;* orcid.org/0000-0002-1271-2019

Complete contact information is available at: https://pubs.acs.org/10.1021/acsnano.1c07705

Author Contributions

M.H.A. and D.A. conceived and designed this experiment. M.H.A conducted sample preparation, material characterization, process development, UV−ozone oxidation, and data analysis. S.C. performed Raman/PL and XPS spectroscopies, acquired AFM images, and contributed to manuscript preparation under supervision of S.K.B. A.R. conducted XPS measurements. X.W. and R.G. conducted memory device fabrication and electrical characterization under the supervision of J.C.L. and D.A. M.A.R. performed UV−ozone oxidation under the supervision of A.D. J.C. performed STEM experiments, and Y.L. conducted CL experiments under the supervision of J.H.W. C.S. and L.H. conducted FIB sample preparation and EEL experiments under the supervision of D.N. R.C. contributed in XPS data analysis under the supervision of F.M. S.R.B. helped in sample preparation. S.J.Y. contributed to AFM scans for step height measurement. M.I.S. helped in XPS data analysis. All authors contributed to the article based on the draft written by M.H.A. and D.A. All authors have approved the final version of the manuscript.

Notes

The authors declare no competing financial interest.

ACKNOWLEDGMENTS

D.A. acknowledges the PECASE award from the Army Research Office (ARO) grant #W911NF-16-1-0277 and the National Science Foundation (NSF) MRSEC Center (DMR-172059). S.K.B. acknowledges support from ARO grant #W911NF-17-1-0312 (MURI) and the NSF NASCENT ERC. The development of the XPS peak fitting model was supported by the Laboratory Directed Research and Development program at Sandia National Laboratories, a multimission laboratory managed and operated by National Technology and Engineering Solutions of Sandia LLC, a wholly owned subsidiary of Honeywell International Inc. for the U.S. Department of Energy's National Nuclear Security Administration under contract DE-NA0003525. The work was partly done at the Texas Nanofabrication Facility supported by NSF grant #NNCI-1542159. The authors would like to thank Haoyue Zhu, Tanushree H. Choudhury, and Joan M. Redwing of 2D Crystal Consortium-Materials Innovation Platform (2DCC-MIP) which is funded by the NSF cooperative agreements DMR-1539916 and DMR-2039351 at Penn State University, for providing the wafer-scale MoS_2 samples. In addition, the authors would like to thank Kun Li of Microelectronics Research Center for taking the optical micrograph of the sapphire wafers. The authors also thank Jo Wozniak of the Texas Advanced Computing Center (TACC) for helping with the three-dimensional renderings.

REFERENCES

(1) Chen, M.; Waghmare, U. V.; Friend, C. M.; Kaxiras, E. A Density Functional Study of Clean and Hydrogen-Covered α-MoO_3 (010): Electronic Structure and Surface Relaxation. *J. Chem. Phys.* **1998**, *109* (16), 6854−6860.

(2) Kihlborg, L. Least Squares Refinement of Crystal Structure of Molybdenum Trioxide. *Arkiv for Kemi* **1963**, *21* (4), 357.

(3) Rahman, F.; Ahmed, T.; Walia, S.; Mayes, E.; Sriram, S.; Bhaskaran, M.; Balendhran, S. Reversible Resistive Switching Behaviour in CVD Grown, Large Area MoO_x. *Nanoscale* **2018**, *10* (42), 19711−19719.

(4) Bessonov, A. A.; Kirikova, M. N.; Petukhov, D. I.; Allen, M.; Ryhänen, T.; Bailey, M. J. Layered Memristive and Memcapacitive Switches for Printable Electronics. *Nature materials* **2015**, *14* (2), 199−204.

(5) Alsaif, M. M.; Chrimes, A. F.; Daeneke, T.; Balendhran, S.; Bellisario, D. O.; Son, Y.; Field, M. R.; Zhang, W.; Nili, H.; Nguyen, E. P.; et al. High-performance Field Effect Transistors Using Electronic Inks of 2D Molybdenum Oxide Nanoflakes. *Adv. Funct. Mater.* **2016**, *26* (1), 91−100.

(6) Bullock, J.; Cuevas, A.; Allen, T.; Battaglia, C. Molybdenum Oxide MoO_x: A Versatile Hole Contact for Silicon Solar Cells. *Appl. Phys. Lett.* **2014**, *105* (23), 232109.

(7) Haber, J.; Lalik, E. Catalytic Properties of MoO_3 Revisited. *Catalysis today* **1997**, *33* (1−3), 119−137.

(8) Fang, S.; Bresser, D.; Passerini, S. Transition Metal Oxide Anodes for Electrochemical Energy Storage in Lithium-and Sodium-ion Batteries. *Adv. Energy Mater.* **2020**, *10* (1), 1902485.

(9) Guo, Y.; Robertson, J. Origin of the High Work Function and High Conductivity of MoO_3. *Appl. Phys. Lett.* **2014**, *105* (22), 222110.

(10) Meyer, J.; Kidambi, P. R.; Bayer, B. C.; Weijtens, C.; Kuhn, A.; Centeno, A.; Pesquera, A.; Zurutuza, A.; Robertson, J.; Hofmann, S. Metal Oxide Induced Charge Transfer Doping and Band Alignment of Graphene Electrodes for Efficient Organic Light Emitting Diodes. *Sci. Rep.* **2015**, *4* (1), 1−7.

(11) Liu, W.; Li, C.; Xu, Q.; Yan, P.; Niu, C.; Shen, Y.; Yuan, P.; Jia, Y. Anderson Localization in 2D Amorphous MoO_{3-x} Monolayers for Electrochemical Ammonia Synthesis. *ChemCatChem.* **2019**, *11* (22), 5412−5416.

(12) Alsaif, M. M.; Balendhran, S.; Field, M. R.; Latham, K.; Wlodarski, W.; Ou, J. Z.; Kalantar-Zadeh, K. Two Dimensional α-MoO_3 Nanoflakes Obtained Using Solvent-Assisted Grinding and Sonication Method: Application for H_2 Gas Sensing. *Sens. Actuators, B* **2014**, *192*, 196−204.

(13) Ji, F.; Ren, X.; Zheng, X.; Liu, Y.; Pang, L.; Jiang, J.; Liu, S. F. 2D-MoO_3 Nanosheets for Superior Gas Sensors. *Nanoscale* **2016**, *8* (16), 8696−8703.

(14) Lee, B. R.; Jung, E. D.; Park, J. S.; Nam, Y. S.; Min, S. H.; Kim, B.-S.; Lee, K.-M.; Jeong, J.-R.; Friend, R. H.; Kim, J.-S.; et al. Highly Efficient Inverted Polymer Light-Emitting Diodes Using Surface Modifications of ZnO Layer. *Nat. Commun.* **2014**, *5* (1), 1−8.

(15) Mai, L. Q.; Hu, B.; Chen, W.; Qi, Y. Y.; Lao, C. S.; Yang, R. S.; Dai, Y.; Wang, Z. L. Lithiated MoO_3 Nanobelts with Greatly Improved Performance for Lithium Batteries. *Adv. Mater.* **2007**, *19* (21), 3712−3716.

(16) Guerfi, A.; Paynter, R. W.; Dao, L. H. Characterization and Stability of Electrochromic MoO_3 Thin Films Prepared by Electrodeposition. *J. Electrochem. Soc.* **1995**, *142* (10), 3457.

(17) Ivanova, T.; Gesheva, K.; Szekeres, A. Structure and Optical Properties of CVD Molybdenum Oxide Films for Electrochromic Application. *J. Solid State Electrochem.* **2002**, *7* (1), 21−24.

(18) Huang, P.-R.; He, Y.; Cao, C.; Lu, Z.-H. Impact of Lattice Distortion and Electron Doping on α-MoO_3 Electronic Structure. *Sci. Rep.* **2015**, *4* (1), 1−7.

(19) Li, F.; Chen, Z. Tuning Electronic and Magnetic Properties of MoO_3 Sheets by Cutting, Hydrogenation, and External Strain: A Computational Investigation. *Nanoscale* **2013**, *5* (12), 5321−5333.

(20) Kalantar-Zadeh, K.; Tang, J.; Wang, M.; Wang, K. L.; Shailos, A.; Galatsis, K.; Kojima, R.; Strong, V.; Lech, A.; Wlodarski, W.; et al. Synthesis of Nanometre-Thick MoO_3 Sheets. *Nanoscale* **2010**, *2* (3), 429−433.

(21) Balendhran, S.; Deng, J.; Ou, J. Z.; Walia, S.; Scott, J.; Tang, J.; Wang, K. L.; Field, M. R.; Russo, S.; Zhuiykov, S.; et al. Enhanced Charge Carrier Mobility in Two-dimensional High Dielectric Molybdenum Oxide. *Adv. Mater.* **2013**, *25* (1), 109−114.

(22) Balendhran, S.; Walia, S.; Alsaif, M.; Nguyen, E. P.; Ou, J. Z.; Zhuiykov, S.; Sriram, S.; Bhaskaran, M.; Kalantar-Zadeh, K. Field Effect Biosensing Platform Based on 2D α-MoO_3. *ACS Nano* **2013**, *7* (11), 9753−9760.

(23) Nicolosi, V.; Chhowalla, M.; Kanatzidis, M. G.; Strano, M. S.; Coleman, J. N. Liquid Exfoliation of Layered Materials. *Science* **2013**, *340* (6139), 1.

(24) Reddy, C. V. S.; Walker, E. H., Jr; Wen, C.; Mho, S. Hydrothermal Synthesis of MoO3 Nanobelts Utilizing Poly (Ethylene Glycol). *J. Power Sources* **2008**, *183* (1), 330−333.

(25) Prasad, A. K.; Kubinski, D. J.; Gouma, P.-I. Comparison of Sol-Gel and Ion Beam Deposited MoO_3 Thin Film Gas Sensors for Selective Ammonia Detection. *Sens. Actuators, B* **2003**, *93* (1−3), 25−30.

(26) Arash, A.; Ahmed, T.; Rajan, A. G.; Walia, S.; Rahman, F.; Mazumder, A.; Ramanathan, R.; Sriram, S.; Bhaskaran, M.; Mayes, E.; et al. Large-Area Synthesis of 2D MoO_{3-x} for Enhanced Optoelectronic Applications. *2D Materials* **2019**, *6* (3), 035031.

(27) Wang, Y.; Du, X.; Wang, J.; Su, M.; Wan, X.; Meng, H.; Xie, W.; Xu, J.; Liu, P. Growth of Large-Scale, Large-Size, Few-Layered α-

MoO_3 on SiO_2 and Its Photoresponse Mechanism. *ACS Appl. Mater. Interfaces* **2017**, *9* (6), 5543−5549.
(28) Hanson, E. D.; Lajaunie, L.; Hao, S.; Myers, B. D.; Shi, F.; Murthy, A. A.; Wolverton, C.; Arenal, R.; Dravid, V. P. Systematic Study of Oxygen Vacancy Tunable Transport Properties of Few-layer MoO_{3-x} Enabled by Vapor-based Synthesis. *Adv. Funct. Mater.* **2017**, *27* (17), 1605380.
(29) Kowalczyk, D. A.; Rogala, M.; Szalowski, K.; Kozlowski, W.; Lutsyk, I.; Piskorski, M.; Krukowski, P.; Dabrowski, P.; Belić, D.; Cichomski, M. Local Electronic Structure of Stable Monolayers of α-MoO_{3-x} Grown on Graphite Substrate. *2D Materials* **2021**, *8* (2), 025005.
(30) Molina-Mendoza, A. J.; Lado, J. L.; Island, J. O.; Niño, M. A.; Aballe, L.; Foerster, M.; Bruno, F. Y.; Lopez-Moreno, A.; Vaquero-Garzon, L.; van der Zant, H. S.; et al. Centimeter-Scale Synthesis of Ultrathin Layered MoO_3 by van Der Waals Epitaxy. *Chem. Mater.* **2016**, *28* (11), 4042−4051.
(31) Du, Y.; Li, G.; Peterson, E. W.; Zhou, J.; Zhang, X.; Mu, R.; Dohnálek, Z.; Bowden, M.; Lyubinetsky, I.; Chambers, S. A. Iso-Oriented Monolayer α-MoO_3 (010) Films Epitaxially Grown on $SrTiO_3$ (001). *Nanoscale* **2016**, *8* (5), 3119−3124.
(32) Altman, E. I.; Droubay, T.; Chambers, S. A. Growth of MoO_3 Films by Oxygen Plasma Assisted Molecular Beam Epitaxy. *Thin Solid Films* **2002**, *414* (2), 205−215.
(33) Bisht, P.; Kumar, A.; Jensen, I. T.; Ahmad, M.; Belle, B. D.; Mehta, B. R. Enhanced Gas Sensing Response for 2D α-MoO_3 Layers: Thickness-Dependent Changes in Defect Concentration, Surface Oxygen Adsorption, and Metal-Metal Oxide Contact. *Sens. Actuators, B* **2021**, *341*, 129953.
(34) Diskus, M.; Nilsen, O.; Fjellvåg, H. Growth of Thin Films of Molybdenum Oxide by Atomic Layer Deposition. *J. Mater. Chem.* **2011**, *21* (3), 705−710.
(35) Yamamoto, M.; Einstein, T. L.; Fuhrer, M. S.; Cullen, W. G. Anisotropic Etching of Atomically Thin MoS_2. *J. Phys. Chem. C* **2013**, *117* (48), 25643−25649.
(36) Park, S.; Garcia-Esparza, A. T.; Abroshan, H.; Abraham, B.; Vinson, J.; Gallo, A.; Nordlund, D.; Park, J.; Kim, T. R.; Vallez, L.; et al. Operando Study of Thermal Oxidation of Monolayer MoS_2. *Advanced Science* **2021**, *8* (9), 2002768.
(37) Kim, H.-U.; Son, J.; Kulkarni, A.; Ahn, C.; Kim, K. S.; Shin, D.; Yeom, G. Y.; Kim, T. Highly Uniform Wafer-Scale Synthesis of α-MoO_3 by Plasma Enhanced Chemical Vapor Deposition. *Nanotechnology* **2017**, *28* (17), 175601.
(38) Nan, H.; Wu, Z.; Jiang, J.; Zafar, A.; You, Y.; Ni, Z. Improving the Electrical Performance of MoS_2 by Mild Oxygen Plasma Treatment. *J. Phys. D: Appl. Phys.* **2017**, *50* (15), 154001.
(39) Zhu, H.; Qin, X.; Cheng, L.; Azcatl, A.; Kim, J.; Wallace, R. M. Remote Plasma Oxidation and Atomic Layer Etching of MoS_2. *ACS Appl. Mater. Interfaces* **2016**, *8* (29), 19119−19126.
(40) Islam, M. R.; Kang, N.; Bhanu, U.; Paudel, H. P.; Erementchouk, M.; Tetard, L.; Leuenberger, M. N.; Khondaker, S. I. Tuning the Electrical Property via Defect Engineering of Single Layer MoS_2 by Oxygen Plasma. *Nanoscale* **2014**, *6* (17), 10033−10039.
(41) Kang, N.; Paudel, H. P.; Leuenberger, M. N.; Tetard, L.; Khondaker, S. I. Photoluminescence Quenching in Single-Layer MoS_2 via Oxygen Plasma Treatment. *J. Phys. Chem. C* **2014**, *118* (36), 21258−21263.
(42) Ko, T. Y.; Jeong, A.; Kim, W.; Lee, J.; Kim, Y.; Lee, J. E.; Ryu, G. H.; Park, K.; Kim, D.; Lee, Z.; et al. On-Stack Two-Dimensional Conversion of MoS_2 into MoO_3. *2D Materials* **2017**, *4* (1), 014003.
(43) Kang, S.; Kim, Y. S.; Jeong, J. H.; Kwon, J.; Kim, J. H.; Jung, Y.; Kim, J. C.; Kim, B.; Bae, S. H.; Huang, P. Y. Enhanced Photoluminescence of Multiple Two-Dimensional van Der Waals Heterostructures Fabricated by Layer-by-Layer Oxidation of MoS_2. *ACS Appl. Mater. Interfaces* **2021**, *13* (1), 1245.
(44) Yang, H. I.; Park, S.; Choi, W. Modification of the Optoelectronic Properties of Two-Dimensional MoS_2 Crystals by Ultraviolet-Ozone Treatment. *Appl. Surf. Sci.* **2018**, *443*, 91−96.
(45) Su, W.; Kumar, N.; Spencer, S. J.; Dai, N.; Roy, D. Transforming Bilayer MoS_2 into Single-Layer with Strong Photoluminescence Using UV-Ozone Oxidation. *Nano Research* **2015**, *8* (12), 3878−3886.
(46) Azcatl, A.; Santosh, K. C.; Peng, X.; Lu, N.; McDonnell, S.; Qin, X.; De Dios, F.; Addou, R.; Kim, J.; Kim, M. J.; et al. HfO_2 on UV-O_3 Exposed Transition Metal Dichalcogenides: Interfacial Reactions Study. *2D Materials* **2015**, *2* (1), 014004.
(47) Jung, C.; Yang, H. I.; Choi, W. Effect of Ultraviolet-Ozone Treatment on MoS_2 Monolayers: Comparison of Chemical-Vapor-Deposited Polycrystalline Thin Films and Mechanically Exfoliated Single Crystal Flakes. *Nanoscale Res. Lett.* **2019**, *14* (1), 1−8.
(48) Novak, T. G.; Kim, J.; Tiwari, A. P.; Kim, J.; Lee, S.; Lee, J.; Jeon, S. 2D MoO_3 Nanosheets Synthesized by Exfoliation and Oxidation of MoS_2 for High Contrast and Fast Response Time Electrochromic Devices. *ACS Sustainable Chem. Eng.* **2020**, *8* (30), 11276−11282.
(49) Bond, T. Ultraviolet-Ozone Surface Treatment. *Three Bond Technol. News* **1987**, *17*, 1−10.
(50) Kc, S.; Longo, R. C.; Wallace, R. M.; Cho, K. Surface Oxidation Energetics and Kinetics on MoS_2 Monolayer. *J. Appl. Phys.* **2015**, *117* (13), 135301.
(51) Liu, X.; Cao, D.; Yang, T.; Li, H.; Ge, H.; Ramos, M.; Peng, Q.; Dearden, A. K.; Cao, Z.; Yang, Y.; et al. Insight into the Structure and Energy of $Mo_{27}S_xO_y$ Clusters. *RSC Adv.* **2017**, *7* (16), 9513−9520.
(52) Sebastian, A.; Pendurthi, R.; Choudhury, T. H.; Redwing, J. M.; Das, S. Benchmarking Monolayer MoS_2 and WS_2 Field-Effect Transistors. *Nat. Commun.* **2021**, *12* (1), 1−12.
(53) Xuan, Y.; Jain, A.; Zafar, S.; Lotfi, R.; Nayir, N.; Wang, Y.; Choudhury, T. H.; Wright, S.; Feraca, J.; Rosenbaum, L.; et al. Multi-Scale Modeling of Gas-Phase Reactions in Metal-Organic Chemical Vapor Deposition Growth of WSe_2. *J. Cryst. Growth* **2019**, *527*, 125247.
(54) Baker, M. A.; Gilmore, R.; Lenardi, C.; Gissler, W. XPS Investigation of Preferential Sputtering of S from MoS_2 and Determination of MoS_x Stoichiometry from Mo and S Peak Positions. *Appl. Surf. Sci.* **1999**, *150* (1), 255−262.
(55) Shimoda, M.; Hirata, T.; Yagisawa, K.; Okochi, M.; Yoshikawa, A. Deconvolution of Mo 3d X-Ray Photoemission Spectraγ-Mo_4O_{11}: Agreement with Prediction from Bond Length-Bond Strength Relationships. *Journal of materials science letters* **1989**, *8* (9), 1089−1091.
(56) Alam, M. H.; Chowdhury, S.; Roy, A.; Braga, M. H.; Banerjee, S. K.; Akinwande, D. Direct Growth of MoS_2 on Electrolytic Substrate and Realization of High-Mobility Transistors. *Physical Review Materials* **2021**, *5* (5), 054003.
(57) Katrib, A.; Stanislaus, A.; Absi-Halabi, M.; Al-Dolama, K. X-Ray Photoelectron Spectroscopy (Xps) Studies of Oxides and Sulphides of Molybdenum and Ni-Mo/Al_2O_3 Hydrodesulphurization Catalysts. *Stud. Surf. Sci. Catal.* **1989**, *53*, 283−299.
(58) Xiong, T.; Zhang, Y.; Wang, Y.; Lee, W. S. V.; Xue, J. Hexagonal MoO_3 as a Zinc Intercalation Anode towards Zinc Metal-Free Zinc-Ion Batteries. *Journal of Materials Chemistry A* **2020**, *8* (18), 9006−9012.
(59) Diehl, R. D.; McGrath, R. Structural Studies of Alkali Metal Adsorption and Coadsorption on Metal Surfaces. *Surf. Sci. Rep.* **1996**, *23* (2−5), 43−171.
(60) Syari'ati, A.; Kumar, S.; Zahid, A.; El Yumin, A. A.; Ye, J.; Rudolf, P. Photoemission Spectroscopy Study of Structural Defects in Molybdenum Disulfide (MoS_2) Grown by Chemical Vapor Deposition (CVD). *Chem. Commun.* **2019**, *55* (70), 10384−10387.
(61) Guimon, C.; Gervasini, A.; Auroux, A. XPS Study of the Adsorption of SO_2 and NH_3 over Supported Tin Dioxide Catalysts Used in De-NOx Catalytic Reaction. *J. Phys. Chem. B* **2001**, *105* (42), 10316−10325.
(62) Levasseur, A.; Vinatier, P.; Gonbeau, D. X-Ray Photoelectron Spectroscopy: A Powerful Tool for a Better Characterization of Thin Film Materials. *Bull. Mater. Sci.* **1999**, *22* (3), 607−614.

(63) Wakabayashi, N.; Smith, H. G.; Nicklow, R. M. Lattice Dynamics of Hexagonal MoS_2 Studied by Neutron Scattering. *Phys. Rev. B* **1975**, *12* (2), 659.
(64) Scanlon, D. O.; Watson, G. W.; Payne, D. J.; Atkinson, G. R.; Egdell, R. G.; Law, D. S. L. Theoretical and Experimental Study of the Electronic Structures of MoO_3 and MoO_2. *J. Phys. Chem. C* **2010**, *114* (10), 4636−4645.
(65) Cai, L.; McClellan, C. J.; Koh, A. L.; Li, H.; Yalon, E.; Pop, E.; Zheng, X. Rapid Flame Synthesis of Atomically Thin MoO_3 down to Monolayer Thickness for Effective Hole Doping of WSe_2. *Nano Lett.* **2017**, *17* (6), 3854−3861.
(66) Heidelmann, M.; Barthel, J.; Houben, L. StripeSTEM, a Technique for the Isochronous Acquisition of High Angle Annular Dark-Field Images and Monolayer Resolved Electron Energy Loss Spectra. *Ultramicroscopy* **2009**, *109* (12), 1447−1452.
(67) Hur, J. H.; Lee, M.-J.; Lee, C. B.; Kim, Y.-B.; Kim, C.-J. Modeling for Bipolar Resistive Memory Switching in Transition-Metal Oxides. *Phys. Rev. B* **2010**, *82* (15), 155321.
(68) Karg, S. F.; Meijer, G. I.; Bednorz, J. G.; Rettner, C. T.; Schrott, A. G.; Joseph, E. A.; Lam, C. H.; Janousch, M.; Staub, U.; La Mattina, F.; Alvarado, S. F.; Widmer, D.; Stutz, R.; Drechsler, U.; Caimi, D. Transition-Metal-Oxide-Based Resistance-Change Memories. *IBM J. Res. Dev.* **2008**, *52* (4.5), 481−492.
(69) Sawa, A. Resistive Switching in Transition Metal Oxides. *Mater. Today* **2008**, *11* (6), 28−36.
(70) Yang, H. I.; Park, S.; Choi, W. Modification of the Optoelectronic Properties of Two-Dimensional MoS_2 Crystals by Ultraviolet-Ozone Treatment. *Appl. Surf. Sci.* **2018**, *443*, 91−96.
(71) Mangolini, F.; Rossi, A.; Spencer, N. D. Chemical Reactivity of Triphenyl Phosphorothionate (TPPT) with Iron: An ATR/FT-IR and XPS Investigation. *J. Phys. Chem. C* **2011**, *115* (4), 1339−1354.
(72) Powell, C. J. The Physical Basis for Quantitative Surface Analysis by Auger Electron Spectroscopy and X-Ray Photoelectron Spectroscopy. *Quantitive Surface Analysis of Materials*; ASTM International, 1978.
(73) Tanuma, S.; Briggs, D.; Grant, J. T. *Electron Attenuation Lengths*; IM Publications, Chichester, UK and Surface Spectra Limited, Manchester UK, 2003; pp 259−294.
(74) Houben, L.; Heidelmann, M.; Gunkel, F. Spatial Resolution and Radiation Damage in Quantitative High-Resolution STEM-EEL Spectroscopy in Oxides. *Micron* **2012**, *43* (4), 532−537.
(75) Ma, X.; Liu, Q.; Xu, D.; Zhu, Y.; Kim, S.; Cui, Y.; Zhong, L.; Liu, M. Capillary-Force-Assisted Clean-Stamp Transfer of Two-Dimensional Materials. *Nano Lett.* **2017**, *17* (11), 6961−6967.
(76) Velický, M.; Donnelly, G. E.; Hendren, W. R.; McFarland, S.; Scullion, D.; DeBenedetti, W. J. I.; Correa, G. C.; Han, Y.; Wain, A. J.; Hines, M. A.; Muller, D. A.; Novoselov, K. S.; Abruña, H. D.; Bowman, R. M.; Santos, E. J. G.; Huang, F. Mechanism of Gold-Assisted Exfoliation of Centimeter-Sized Transition-Metal Dichalcogenide Monolayers. *ACS Nano* **2018**, *12* (10), 10463−10472.

https://doi.org/10.1021/acsnano.1c07705
ACS Nano 2022, 16, 3756−3767